



HAL
open science

Second harmonic generation in the presence of walk-off and group velocity mismatch

Marc Hanna, Michele Natile, Yoann Zaouter, Manuel Joffre, Patrick Georges

► **To cite this version:**

Marc Hanna, Michele Natile, Yoann Zaouter, Manuel Joffre, Patrick Georges. Second harmonic generation in the presence of walk-off and group velocity mismatch. *Journal of the Optical Society of America B*, 2023, 40 (5), pp.930-938. 10.1364/josab.485597. hal-04072421

HAL Id: hal-04072421

<https://iogs.hal.science/hal-04072421v1>

Submitted on 20 Apr 2023

HAL is a multi-disciplinary open access archive for the deposit and dissemination of scientific research documents, whether they are published or not. The documents may come from teaching and research institutions in France or abroad, or from public or private research centers.

L'archive ouverte pluridisciplinaire **HAL**, est destinée au dépôt et à la diffusion de documents scientifiques de niveau recherche, publiés ou non, émanant des établissements d'enseignement et de recherche français ou étrangers, des laboratoires publics ou privés.

Second harmonic generation in the presence of walk-off and group velocity mismatch

MARC HANNA^{1,*}, MICHELE NATILE², YOANN ZAOUTER², MANUEL JOFFRE³, PATRICK GEORGES¹

¹Université Paris-Saclay, Institut d'Optique Graduate School, CNRS, Laboratoire Charles Fabry, 91127 Palaiseau, France

²Amplitude, 11 Avenue de Canteranne, Cité de la Photonique, 33600 Pessac, France

³Laboratoire d'Optique et Biosciences, Ecole Polytechnique, CNRS, INSERM, Institut Polytechnique de Paris, 91128 Palaiseau, France

*marc.hanna@institutoptique.fr

Abstract: We study a second-harmonic generation interaction geometry in the case where both group velocity mismatch and walk-off have significant impact. This results in a frequency-converted beam exhibiting pulse front tilt. Using the global response function of the crystal, we provide an analytical model that allows to predict the spatio-temporal structure of the second-harmonic wavepacket and verify its validity using numerical simulations and a simple experiment. Distinctive features of this geometry are the suppression of back-conversion and the ability to conserve the fundamental bandwidth in the space and time domains. Subsequent compensation of the pulse front tilt should allow efficient generation of ultrashort pulses in the deep ultraviolet.

© 2023 Optica Publishing Group

1. Introduction

Second harmonic generation (SHG) was the first nonlinear optical phenomenon to be observed shortly after the invention of the laser [1]. Since then, it has proven invaluable to generate coherent radiation in wavelength ranges where available laser materials exhibit mediocre properties or are simply not available, in temporal regimes ranging from CW to femtosecond pulses. In particular, mature laser technologies generating beams in the near infrared based on neodymium- or ytterbium-doped materials can be used to produce high-power sources of light in the visible or UV ranges [2–4], after wavelength conversion through SHG. The efficiency of the process and the properties of the interaction and converted beams have been quite extensively described since the 1960s [5].

Two phenomena, walk-off and group-velocity mismatch (GVM), are essential in understanding SHG of short pulses that are tightly focused onto the nonlinear material. They are closely related and can be seen as dual versions in the space and time domains of the same effect [6]: walk-off is related to the first-order dependence of fundamental and/or second-harmonic wavevectors with respect to angular deviations (or equivalently transverse component of the wavevector) from the phase-matching angle. GVM is related to the first-order dependence of these same wavevectors with respect to optical frequencies. Walk-off and GVM are also closely related to the notions of angular and spectral acceptance respectively.

Theoretical descriptions and consequences of these effects have been available for decades in various levels of complexity. Since the first formalism describing SHG with focused Gaussian beam that included walk-off [5], other models have been developed to take into account GVM alone [7, 8]. An analytical model for the efficiency of SHG that takes both GVM and walk-off into account was also published in 2003 [9]. However, this work does not establish the space-time structure of the SHG beam, nor does it allow to predict its spatial and spectral widths.

Here we present a simple model that allows to predict the coupled space-time structure of the SHG beam in the presence of both walk-off and GVM. Although it has been recognized in

46 the context of pulse characterization techniques [10] that the simultaneous presence of these
 47 effects leads to pulse front tilt (PFT), or equivalently angular dispersion, the implications have not
 48 been examined for SHG to our knowledge. Our model is established in the spatial and temporal
 49 frequency domain [6], as opposed to previous descriptions in the space / time domain [5, 7–9]. It
 50 matches the predictions of previous approaches, and also yields the explicit analytical solution
 51 which allows to predict SHG bandwidths, efficiency, and spatio-temporal beam structure in a rather
 52 general case, providing an analytical ground for what has been observed experimentally [11, 12].
 53 One important consequence is that in the presence of strong GVM and walk-off, back conversion
 54 to the fundamental beam is suppressed in both the space and time domains, allowing to reach
 55 large conversion efficiencies. Full 3D numerical simulations are performed to confirm the validity
 56 of this model, making it a useful tool to design efficient frequency conversion stages for ultrashort
 57 pulses, and an experimental confirmation of the presence of strong space-time couplings in the
 58 SHG beam is presented. Practical consequences are expected to be important for the generation
 59 of short pulses in the UV and DUV ranges, where both walk-off and GVM parameters have
 60 large values, with possible applications to material processing and experiments involving the
 61 generation of photoelectrons.

62 2. Intuitive description in the space-time domain

63 A simple picture in the space-time domain allows to establish the presence of PFT in the SHG
 64 beam and determine its value, as shown in Fig. 1. Consider an input fundamental wavepacket
 65 entering at the left side of the nonlinear crystal that exhibits both walk-off and GVM. During
 66 propagation, at each location, this wavepacket triggers a second order polarization that radiates
 67 the SHG beam. This beam propagates at a usually lower group velocity, at an angle determined
 68 by the walk-off in the considered crystal. Fig. 1 shows in red the position of these individual
 69 SHG beamlets at the time corresponding to the fundamental beam leaving the nonlinear crystal.
 70 These beamlets are arranged in a line, with a PFT angle γ given by

$$\tan \gamma = \frac{v_{g1} - v_{g2} \cos \rho}{v_{g2} \sin \rho}, \quad (1)$$

71 where ρ is the walk-off angle, and v_{g1} and v_{g2} are the group velocities of the fundamental and
 72 SHG pulses respectively. For sufficiently small values of the walk-off angle, this reduces to

$$\tan \gamma \approx v_{g1} \frac{\text{GVM}}{\rho}, \quad (2)$$

73 where the GVM parameter is defined by $\text{GVM} = 1/v_{g2} - 1/v_{g1}$. The factor GVM/ρ is the PFT
 74 parameter in units of s/m, and only depends on the phase matching geometry. The presence
 75 of PFT in the SHG beam is, to our knowledge, not mentioned in previous papers describing
 76 efficient generation using thick crystals where GVM and walk-off are both present [11, 12]. In
 77 general, when the SHG beam quality and SHG efficiency is the major concern, configurations
 78 with large GVM or walk-off are avoided. It is however at the basis of some pulse characterization
 79 techniques that use sum-frequency mixing [10]. Although the PFT can hinder further applications,
 80 it is well known that it is equivalent to angular dispersion [13, 14], and can be controlled, and
 81 removed, using angularly dispersive optical components such as prisms and gratings. This would
 82 correspond to the inverse of a technique that has been studied over the last 25 years [15–19],
 83 where the idea is to generate SHG or perform another nonlinear frequency mixing from an input
 84 pulse exhibiting PFT, in order to maximize the phase-matching bandwidth.

85 Although this simple picture in the time-space domain allows to evaluate the PFT and PFT
 86 angles, it remains unclear what the detailed structure of the SHG beam is. For instance, what is
 87 its optical bandwidth, or how does this beam diffract in the far field? To get more insight into this
 88 process, and be able to predict such properties, we now describe this interaction in more details
 89 using a simple analytical model.

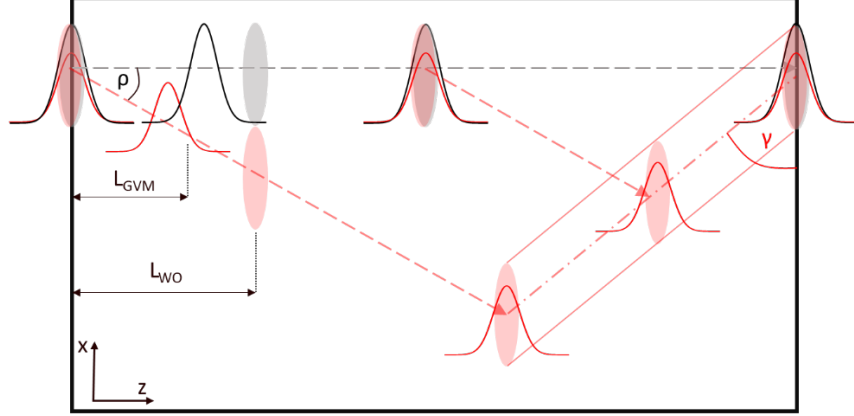


Fig. 1. Illustration of the origin of the pulse front tilt in the SHG beam in the presence of GVM and walk-off. The black/grey colors are associated to the fundamental beam, and the red color is associated to the SHG beamlets. The GVM and walk-off characteristic lengths, corresponding to separation of the fundamental and SHG wavepackets in time and space respectively, are also illustrated (respectively L_{GVM} and L_{WO}).

90 3. Simple model in the wavevector-spectral domain

91 The model we develop here is based on the spatio-temporal generalization of the global
 92 multidimensional response function, hereafter denoted Ξ . This approach, discussed earlier
 93 within the plane-wave approximation [20], has been used previously in the context of broadband
 94 SHG [21] and multidimensional spectroscopy [22,23]. While a complete theoretical development
 95 is provided in the Appendix, this section focuses on the most relevant physical effects. As shown
 96 in Fig. 1, we assume that the fundamental and SHG pulses propagate in the z direction, and we
 97 keep only one spatial transverse dimension, x , chosen so that the xz plane contains the optical
 98 axis. The complex electric field is written as a function of its 2D Fourier transform according to

$$E_\ell(z, x, t) = \iint E_\ell(z, k_x, \omega) e^{i(k_x x - \omega t)} \frac{dk_x}{2\pi} \frac{d\omega}{2\pi}, \quad (3)$$

99 with $\ell = 1$ for the fundamental and $\ell = 2$ for the second harmonic. Second-order effects such
 100 as diffraction in the space domain or group-velocity dispersion (GVD) in the time domain are
 101 neglected for simplicity, although they can be readily included as shown in the Appendix. Pump
 102 depletion is also neglected so that propagation of the fundamental pulse complex field is simply
 103 described by

$$E_1(z, k_x, \omega) = E_1(0, k_x, \omega) \exp(ik_1(k_x, \omega)z), \quad (4)$$

104 where k_1 is the wavevector of the fundamental wavepacket. We write the second-harmonic complex
 105 field as $E_2(z, k_x, \omega) = A_2(z, k_x, \omega) \exp(ik_2(k_x, \omega)z)$, where $k_2(k_x, \omega)$ is the wavevector of
 106 the SHG wavepacket, and $A_2(z, k_x, \omega)$ is a slowly-varying envelope. As shown in the Appendix,
 107 the propagation of the SHG pulse is described within the paraxial wave approximation by

$$\frac{\partial A_2(z, k_x, \omega)}{\partial z} = \frac{i\omega}{2n_2\epsilon_0 c} P^{(2)}(z, k_x, \omega) \exp(-ik_2(k_x, \omega)z), \quad (5)$$

108 where n_2 is the refractive index at the SHG center frequency, ϵ_0 is the vacuum permittivity, and c
 109 is the speed of light in vacuum. The second-order nonlinear polarization $P^{(2)}$ is given by:

$$P^{(2)}(z, x, t) = -\frac{\epsilon_0 \chi^{(2)}}{2} E_1^2(z, x, t). \quad (6)$$

Fourier transform and substitution of this expression in the propagation equation (5) leads, after integrating over z , to the following expression for the SHG pulse envelope

$$A_2(z, k_x, \omega) = \iint \Xi(k_x, k_{x1}, \omega, \omega_1) E_1(k_{x1}, \omega_1) E_1(k_x - k_{x1}, \omega - \omega_1) \frac{dk_{x1}}{2\pi} \frac{d\omega_1}{2\pi}, \quad (7)$$

110 where the dropped dependence on z in E_1 means that it is taken at $z = 0$. In the above equation,
111 we have introduced the multidimensional spatio-temporal response function $\Xi(k_x, k_{x1}, \omega, \omega_1)$,
112 expressed below as a function of the wavevector mismatch, Δk :

$$\Xi(k_x, k_{x1}, \omega, \omega_1) = \frac{i\omega\chi^{(2)} \exp(i\Delta k(k_x, k_{x1}, \omega, \omega_1) z) - 1}{4n_2c \ i\Delta k(k_x, k_{x1}, \omega, \omega_1)}. \quad (8)$$

113 The wavevector mismatch Δk is itself defined as

$$\Delta k(k_x, k_{x1}, \omega, \omega_1) = k_1(k_{x1}, \omega_1) + k_1(k_x - k_{x1}, \omega - \omega_1) - k_2(k_x, \omega). \quad (9)$$

114 The result of Eq. (7) is somewhat similar to previous approaches [5, 9] but is formulated here in
115 Fourier space. We now start by assuming perfect phase matching ($\Delta k = 0$) as a reference point
116 for later derivations. In this case, $\Xi = i\omega\chi^{(2)}z/(4n_2c)$ and the second harmonic pulse is simply
117 given by

$$A_{2,PM}(z, k_x, \omega) = z \frac{i\omega\chi^{(2)}}{4n_2c} \iint E_1(k_{x1}, \omega_1) E_1(k_x - k_{x1}, \omega - \omega_1) \frac{dk_{x1}}{2\pi} \frac{d\omega_1}{2\pi}. \quad (10)$$

118 We recover the fact that the intensity of the SHG beam grows like z^2 . SHG can be interpreted as
119 a summation of sum-frequency processes both in the temporal and spatial frequency domains. In
120 the case where the fundamental wavepacket E_1 is a Gaussian function in space and time, the
121 autoconvolution operation results in a SHG pulse with a spectral width multiplied by $\sqrt{2}$, and a
122 spatial frequency width multiplied by the same factor. This corresponds to a pulsewidth and a
123 beam radius divided by $\sqrt{2}$, a well-known result that stems from the quadratic polarization term.

124 Let us now consider the case where the wavevectors exhibit first-order dependencies on ω and
125 k_x as follows:

$$k_1(k_x, \omega) = k_1(\omega_0) + \frac{\partial k_1}{\partial \omega}(\omega - \omega_0) \quad (11)$$

126

$$k_2(k_x, \omega) = k_2(2\omega_0) + \frac{\partial k_2}{\partial \omega}(\omega - 2\omega_0) + \frac{\partial k_2}{\partial k_x}k_x. \quad (12)$$

127 In this case, for simplicity, we have considered a type I (ooe) SHG where the fundamental beam
128 is polarized along the ordinary axis of the nonlinear crystal, so that its k-vector does not depend
129 on k_x or equivalently the phase matching angle. However, the SHG beam is polarized along the
130 extraordinary axis, and therefore exhibits walk-off. Note that this analysis can be extended to
131 other phase-matching geometries. The phase mismatch is thus given by:

$$\Delta k(k_x, k_{x1}, \omega, \omega_1) = \left(\frac{\partial k_1}{\partial \omega} - \frac{\partial k_2}{\partial \omega} \right) (\omega - 2\omega_0) - \frac{\partial k_2}{\partial k_x} k_x = GVM \times \Omega - \rho \times k_x, \quad (13)$$

132 where we have identified the GVM parameter and walk-off angle, and $\Omega = \omega - 2\omega_0$. We
133 can see that, to first order, Δk does not depend on ω_1 and k_{x1} , so that the response function
134 $\Xi(k_x, k_{x1}, \omega, \omega_1) = \Xi(k_x, \omega)$ can be taken out of the integral in Eq. (7). The response function
135 then merely acts as a filter that will attenuate (k_x, Ω) components that are not phase matched.
136 As a result, the emitted SHG field can be written as:

$$A_2(z, k_x, \Omega) = A_{2,PM}(z, k_x, \Omega) \exp\left(i\frac{\Delta k z}{2}\right) \text{sinc}\left(\frac{\Delta k z}{2}\right). \quad (14)$$

137 The SHG field can therefore be decomposed into the product of the perfectly phase-matched
 138 result, that occupies a region of the (k_x, Ω) space, with the standard sinc function describing
 139 phase matching effects. The additional phase term is linear in ω and k_x , and therefore simply
 140 corresponds to a shift in the time and space domains. To determine the region of the (k_x, Ω)
 141 space that corresponds to perfect phase matching, we set $\Delta k = 0$ and find

$$k_x = \frac{GVM}{\rho} \Omega, \quad (15)$$

142 describing a linear angular dispersion that is coherent with the PFT established in Eq. (2).

143 3.1. Spectral and wavevector widths

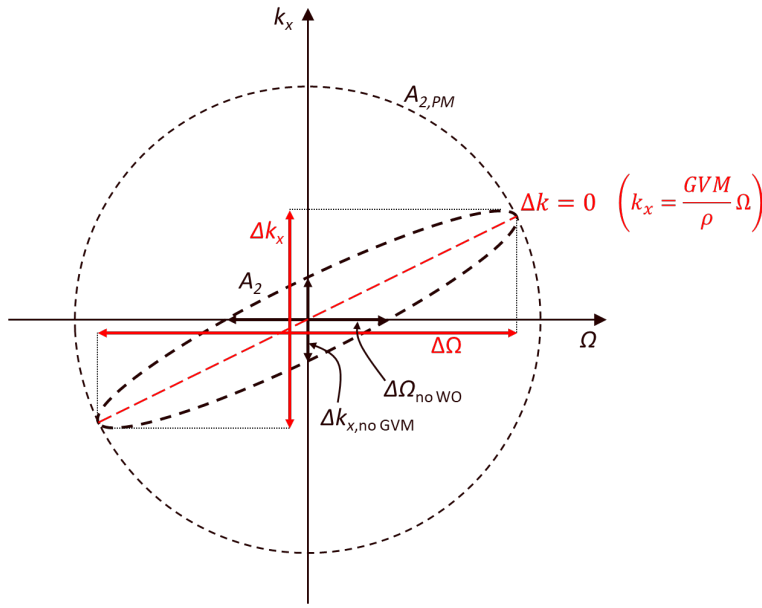


Fig. 2. Schematic of the (k_x, Ω) plane showing the extent of the second-order polarization term resulting in $A_{2,PM}$ and the $\Delta k = 0$ line in the presence of both walk-off and GVM. The dashed-line ellipse represents schematically A_2 , obtained by multiplying $A_{2,PM}$ by the response function. The different spectral and angular widths are also shown.

144 In addition to recovering this result, this simple model allows to compute the overall widths of
 145 the radiated SHG beam. For this, Fig. 2 helps visualizing the situation in the (k_x, Ω) domain.
 146 The spatio-temporal response function $\text{sinc}(\Delta k z/2)$ acts as a filter in the (k_x, Ω) plane, resulting
 147 in the SHG field represented by the dashed-line ellipse. Let us assume that the input fundamental
 148 beam is Gaussian in space and time:

$$E_1(x, t) \propto \exp\left(-\frac{t^2}{2\Delta t^2} - \frac{x^2}{2\Delta x^2} - i\omega_0 t\right) \longleftrightarrow E_1(k_x, \Omega) \propto \exp\left(-\frac{(\omega - \omega_0)^2}{2\Delta\omega^2} - \frac{k_x^2}{2\Delta k_x^2}\right), \quad (16)$$

149 with widths in the space and time domains verifying $\Delta t \Delta\omega = 1$ and $\Delta x \Delta k_x = 1$. The
 150 experimentally used full width at half maximum (FWHM) pulse duration Δt_{FWHM} and beam
 151 waist radius w are related to these widths by $\Delta t_{FWHM} = 2\sqrt{\ln 2} \Delta t$ and $w = \sqrt{2} \Delta x$. As already

152 mentioned, in this case, the perfectly phase matched SHG field is given by the autoconvolution of
 153 the 2D Gaussian function, and therefore

$$|A_{2,PM}(z, k_x, \Omega)|^2 \propto \exp\left(-\frac{\Omega^2}{2\Delta\omega^2} - \frac{k_x^2}{2\Delta k_x^2}\right). \quad (17)$$

154 The coordinates of half intensity of this pulse in the 2D (k_x, Ω) plane are given by

$$\Delta t^2 \Omega^2 + \Delta x^2 k_x^2 = 2\ln 2 \quad (18)$$

155 The overall full widths at half maximum (FWHM) in the Fourier domains are obtained along the
 156 $\Delta k = 0$ line, yielding the following results:

$$\Delta\Omega_{FWHM} = \frac{2\sqrt{2\ln 2}}{\sqrt{\Delta t^2 + GVM^2 \frac{\Delta x^2}{\rho^2}}} \quad (19)$$

157

$$\Delta k_x_{FWHM} = \frac{2\sqrt{2\ln 2}}{\sqrt{\Delta x^2 + \rho^2 \frac{\Delta t^2}{GVM^2}}}. \quad (20)$$

158 These equations formally establish an experimental observation that was reported several
 159 times [7, 12] with the following qualitative argument: in the presence of significant walk-off,
 160 instead of being determined by the overall nonlinear medium length, the spectral width is related
 161 to the walk-off length $L_{WO} = \Delta x/\rho$, because the fundamental and SHG fields interact coherently
 162 only over this distance. Symmetrically, the angular spectrum is determined by the GVM length
 163 $L_{GVM} = \Delta t/GVM$.

164 If we assume $k_x = 0$, corresponding to a large, collimated beam for which walk-off can be
 165 neglected, the spectral acceptance is limited by the sinc term instead of the input beam imprint in
 166 the (k_x, Ω) plane along the $\Delta k = 0$ line. In this case we recover the usual spectral acceptance

$$\Delta\Omega_{\text{no WO}} = \frac{2\pi \cdot 0.886}{GVM L}, \quad (21)$$

167 where L is the crystal length. Similarly, if we assume $\Omega = 0$, corresponding to a narrowband
 168 fundamental pulse, the angular acceptance is given by

$$\Delta k_x_{\text{no GVM}} = \frac{2\pi \cdot 0.886}{\rho L}. \quad (22)$$

169 3.2. Efficiency

170 This simple model also allows to evaluate the efficiency in the simultaneous presence of GVM
 171 and walk-off, a question that was already answered in previous work [9]. Here we show that the
 172 results are coherent with the literature and cast in a way that makes the symmetry between time
 173 and space clearer. To compute the efficiency, we must take the magnitude squared of Eq. (14)
 174 and integrate it over Ω and k_x . We define the efficiency of the perfectly phase-matched process as
 175 $\eta_{PM} = \eta_0 L^2$, and assume that the distribution of the wavepacket in the (k_x, Ω) plane is separable
 176 as a Gaussian function along the ellipse major axis and a sinc function along the minor axis. This
 177 is equivalent to saying that at least one of the effects, among WO and GVM, is strong enough to
 178 significantly reduce the spectral or angular acceptance. In this case the efficiency is found to be
 179 given by

$$\eta = \sqrt{2\pi}\eta_0 \frac{L_{WO}L_{GVM}}{\sqrt{L_{WO}^2 + L_{GVM}^2}} L. \quad (23)$$

180 The efficiency is now linear with propagation distance, a well-known result, and limited by
181 an effective coherent interaction length that depends symmetrically on the walk-off and GVM
182 lengths. We now turn to numerical simulations to validate the predictions of this simple model
183 both in terms of the amount of PFT present in the output SHG beam and its angular and spectral
184 distribution.

185 4. Numerical simulations

186 The numerical model is based on two envelope propagation equations [24] for the fundamental and
187 SHG beams respectively, coupled through the second-order nonlinear polarization corresponding
188 to the specific wave-mixing of interest. These fields are three-dimensional $E(x,y,t)$ and propagated
189 in the direction z using a split-step Fourier method: linear effects such as diffraction and dispersion
190 are accounted for in the Fourier domain, while nonlinear effects are implemented in the direct
191 space, over successive longitudinal propagation steps [25]. The wavevectors dependence on
192 frequency and angle for each field are calculated using the full Sellmeier equations of the
193 considered material [26]. This results in a model where dispersion to all orders (therefore
194 including phase matching, GVM and GVD), walk-off, diffraction, and second-order nonlinear
195 effects are completely taken into account. Pump depletion will therefore be observed for a
196 sufficiently efficient interaction. Third-order nonlinear effects are also included but play a
197 negligible role at the considered intensities.

198 As a starting point, we consider an input Gaussian fundamental pulse at 515 nm with a FWHM
199 pulsewidth of 300 fs, and a beam waist radius (at $1/e^2$ in intensity) of 25 μm located at the center
200 of the crystal. This pulse is launched into an 8 mm-long BBO crystal at a phase matching angle
201 of $\theta=49.8^\circ$, corresponding to type I (ooe) phase matching for SHG. The confocal parameter
202 corresponding to this pump beam radius in the crystal is 12.6 mm, while the GVD values at the
203 pump and SHG wavelengths are 140 fs^2/mm and 460 fs^2/mm . As a result, diffraction and GVD
204 have a limited impact on propagation.

205 The GVM parameter and walk-off angle in this situation are 630 fs/mm and 85 mrad. Over the
206 8 mm-long crystal, this translates into a delay between fundamental and SHG pulses of 5 ps and
207 an overall lateral beam displacement of 680 μm , corresponding to very pronounced GVM and
208 walk-off effects.

209
210 Figure 3 shows the spatio-temporal structure of the output SHG beam, along with integrated
211 profiles in the time domain and along the critical phase matching direction x , obtained both from
212 the analytical analysis of section 3 using Eq. (14), and from the full simulation with a very low
213 input energy of 0.1 nJ, where pump depletion is negligible. The pulse front tilt expected from
214 the simple argument of section 2 is clearly observed, with a PFT of 7.4 ps/mm. The analytical
215 and simulation results are in very good agreement, except for the signal enhancement around
216 $x = 0$ (and hence $t = 0$) due to pump beam size variations that are not taken into account in
217 the analytical model. The observed linear coupling in the space-time domain is mirrored in the
218 Fourier space-time domain, corresponding to angular dispersion.

219 In the remainder of this section, the input pulse energy is set to 5 nJ. The simulation results
220 are shown in Fig. 4. In this case, in addition to the spatio-temporal structure, pump depletion
221 causes the intensity of the SHG beam to increase gradually over time, because the SHG beamlets
222 generated at the beginning of propagation, when the pump intensity is the highest, are delayed the
223 most. In this case, the overall efficiency is 56%. This high value illustrates a distinctive feature
224 of this frequency conversion geometry: because GVM and walk-off separate the fundamental
225 and SHG radiations in time and space over rather small propagation distances compared to the
226 crystal length, back-conversion, which supposes a coherent interaction, is suppressed.

227 The output SHG beam profiles in the near and far fields are shown in Fig. 5. As expected, the
228 SHG beam at the output facet of the crystal exhibits a strongly asymmetric beam profile induced

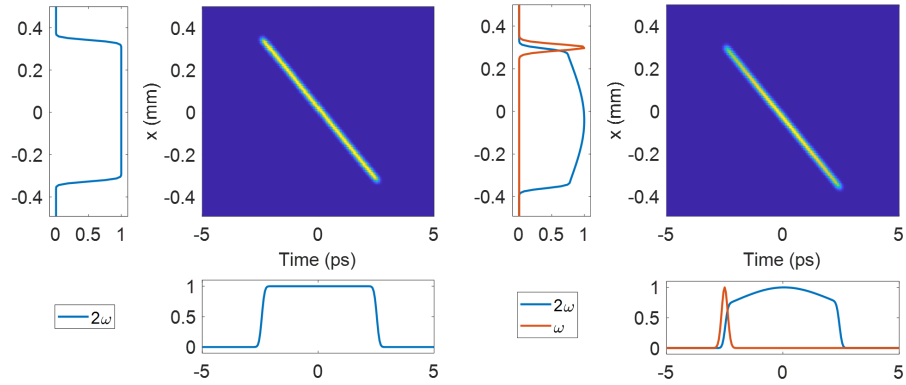


Fig. 3. Left: Spatio-temporal structure of the output SHG beam obtained from the analytical model (Fourier transform of Eq. (14)), and projections on the time and space axes (blue). Right: Same plot obtained from full numerical simulations at an input energy of 0.1 nJ, the red curve corresponds to the fundamental pulse at the output of the crystal.

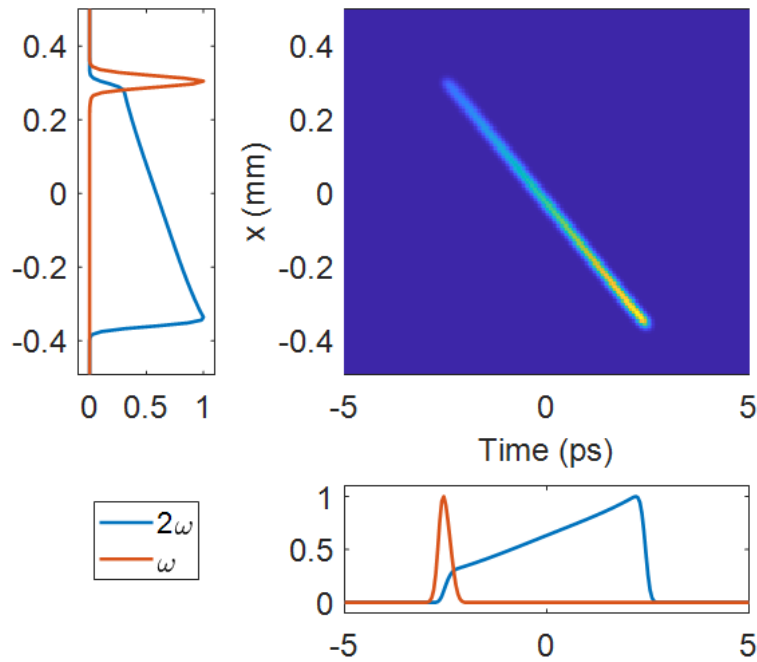


Fig. 4. Spatio-temporal structure of the output SHG beam obtained from full numerical simulations at an input energy of 5 nJ, and projections on the time and space axes (blue). The red curve corresponds to the fundamental pulse at the output of the crystal.

229 by the walk-off. However, contrary to the situation where GVM is negligible, this elongated
 230 profile in the near field does not translate into an equivalently elongated profile in the far field,

231 with interchanged axes. The reason for this was identified, for example in [16]: because of the
 232 space-time coupling, wavepackets with PFT exhibit diffraction properties that are related to the
 233 instantaneous size of the beam rather than the time-integrated one, leading to stronger diffraction.

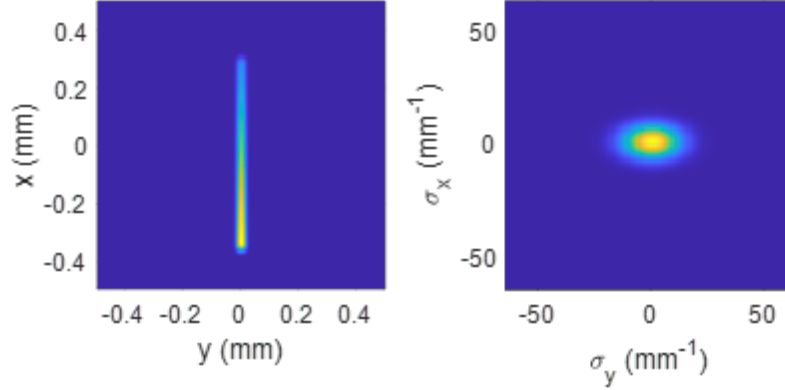


Fig. 5. Output SHG beam (left) and corresponding far field (right).

234 To get more physical insight into the behavior of SHG output spectral width and far-field width
 235 as a function of input parameters of the pump pulse such as pulsewidth and beam size, the model
 236 is used repeatedly while scanning one parameter. From the starting point, we first vary the input
 237 beam radius with values of 25 μm , 50 μm , and 100 μm . To keep the peak intensity constant,
 238 the pump pulse energy is set to 5 nJ, 20 nJ, and 80 nJ respectively. The SHG output spectrum,
 239 integrated over space, is shown in Fig. 6 (left). As expected from the analytical analysis, the
 240 spectral width is reduced as the input beam size increases, with values of 0.35 nm, 0.24 nm,
 241 and 0.14 nm. The results given by Eq. (19) are 0.37 nm, 0.26 nm, and 0.14 nm, in excellent
 242 agreement. For these situations where the walk-off displacement is much larger than the input
 243 beam size, the spectral width scales like the inverse of the input beam size. This is in line
 244 with experimental observations [7, 12], and the following explanation: as the length over which
 245 fundamental and SHG radiations interact coherently in the space domain L_{WO} increases, the
 246 spectral width is reduced because of the limited spectral acceptance of the crystal. However, for
 247 small initial beam sizes, the SHG pulse can be generated over the full input bandwidth, yielding
 248 a way to efficiently convert short pulses even in the presence of a large GVM, or equivalently a
 249 small spectral acceptance.

250 Symmetrically, from the starting point, we vary the pump pulsewidth with values of 300 fs,
 251 600 fs, and 1200 fs, and pulse energies scaled to 5 nJ, 10 nJ, and 20 nJ respectively. Figure 6
 252 (right) shows the time-integrated SHG far fields, yielding a result expected from Eq. (20): as the
 253 length over which fundamental and SHG radiations interact coherently in the time domain L_{GVM}
 254 increases, the angular width is reduced because of the limited angular acceptance of the crystal.
 255 However the full input wavevector spectrum can be converted if a sufficiently small pulsewidth
 256 is used at the input. The spatial frequency FWHM observed in simulations are 12 mm^{-1} , 7.0
 257 mm^{-1} and 3.8 mm^{-1} , while Eq. (20) yields values of 12 mm^{-1} , 7.2 mm^{-1} , and 3.8 mm^{-1} , again
 258 in excellent agreement.

259 5. Experimental confirmation of the presence of angular dispersion

260 Finally, we perform an experiment to evidence the presence of PFT, or equivalently angular
 261 dispersion, in the output SHG beams when both GVM and walk-off play an important role.
 262 Starting from an ytterbium-doped femtosecond laser system at 1030 nm, we generate 300 fs

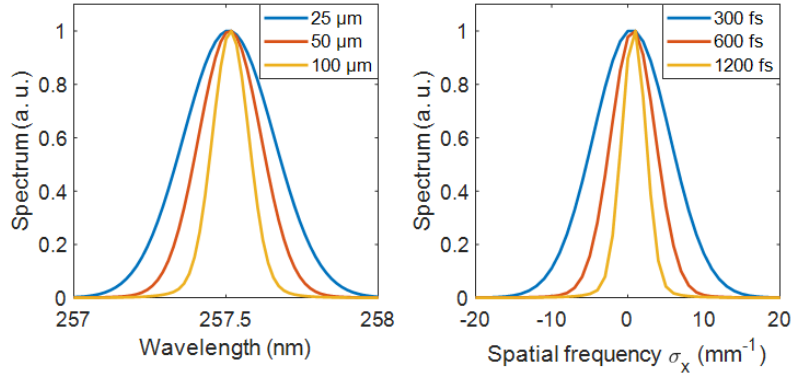


Fig. 6. Output SHG spectrum for input beam radii of 25, 50, and 100 μm (left). Output SHG wavevector spectrum for input pulse durations of 300, 600, and 1200 fs (right)

263 pulses at 515 nm in a first type I SHG stage using a 4 mm-long LBO crystal. These pulses are
 264 then focused onto a beam diameter of approximately 60 μm inside a 9.4 mm-long BBO crystal
 265 cut for type I SHG at 515 nm to generate a beam at 257 nm. These conditions approximately
 266 match the situation considered in the numerical simulations section.

267 The near field of the beam generated at 257 nm is measured by imaging the output facet of the
 268 nonlinear crystal onto a camera, and is displayed in Fig. 7. The strong beam asymmetry shown
 269 by the simulation in Fig. 5 is clearly observed. The spot that appears on top of the line is the
 270 fundamental beam at 515 nm. The far-field, measured using the same camera by removing the
 271 imaging lens, is shown in Fig. 7, and is also in qualitative agreement with the simulations. In
 272 particular, the difference in size between the vertical and horizontal directions is not at all as
 273 pronounced as in the near-field, because of the presence of strong spatio-temporal couplings.

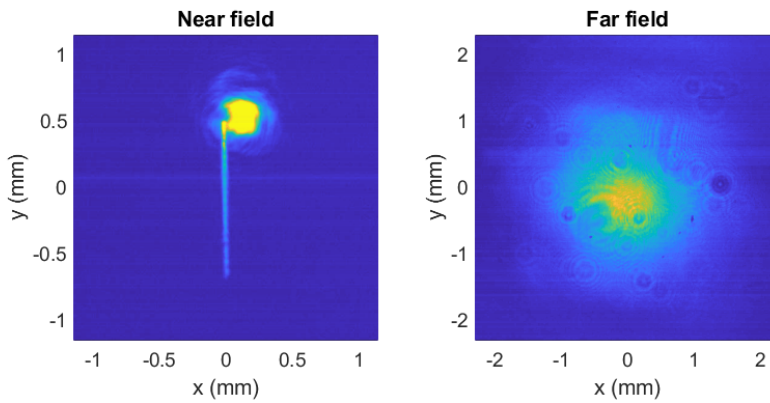


Fig. 7. Measured near-field (left) and far-field (right) profiles of the DUV beam.

274 To obtain a quantitative estimation of the PFT, we let the generated UV beam propagate to
 275 the far field and a spectrometer coupled to a 50 μm diameter multimode fiber mounted on a
 276 translation stage is positioned 31 cm away from the crystal. This allows to measure the spatial
 277 chirp at this location, a consequence of the angular dispersion. The data is plotted as spectra as a
 278 function of deviation angle from the beam center.

279 Figure 8 shows the result of this measurement. The left panel shows that the central wavelength

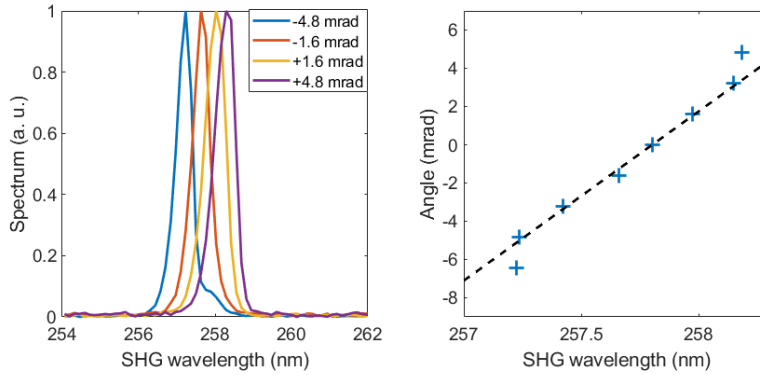


Fig. 8. Left: Measured SHG spectra in the far field at deviations angle varying from -4.8 mrad to +4.8 mrad from the optical axis in the critical phase matching plane. Right: deviation angle as a function of centroid wavelength, with a slope of 9.0 mrad/nm.

280 shifts as the fiber is translated in the UV beam, as expected for an angularly dispersed beam.
 281 The right panel shows the angular deviation as a function of centroid wavelength, with an
 282 experimentally measured angular dispersion of 9.0 mrad/nm. This value is very close to the
 283 theoretically expected one of $\partial\theta/\partial\lambda = PFT \times c/\lambda_0 = 8.6$ mrad/nm. This simple experiment
 284 therefore confirms the spatio-temporal structure of the SHG beam.

285 6. Conclusion

286 To conclude, we have presented an analytical model that predicts the spatio-temporal structure
 287 of SHG beams when both GVM and walk-off play a significant role. We show that a pulse
 288 front tilt is imparted onto the beam, as the fundamental and SHG wavepackets separate in both
 289 space and time. This separation implies that the coherent interaction length is limited both in
 290 the time and space domains, therefore suppressing the possibility for back conversion. As a
 291 result, it is possible to obtain high SHG efficiencies using this scheme, even for pulses exhibiting
 292 a bandwidth that exceeds the spectral acceptance of the crystal. The output beam PFT can be
 293 compensated using standard optical elements that introduce angular dispersion such as gratings
 294 and prisms. When pump depletion is negligible, the output pulses exhibit a square-shaped profile
 295 in the time domain and in the direction of critical phase-matching. The onset of pump depletion
 296 causes these profiles to become inhomogeneous. To generate more spatially symmetric profiles,
 297 beam reshaping techniques using e. g. cylindrical lenses could be used.

298 This nonlinear interaction geometry bears some similarities with broadband phase matching
 299 techniques based on the introduction of pulse front tilt in the input interacting beams. These
 300 techniques also require compensation of the output PFT in the generated beam. However, in the
 301 case studied here, there is no need for spatio-temporal beam management of the input pulses.
 302 The lack of back-conversion is also a distinctive feature, that avoids bandwidth-limiting effects
 303 and related spectral and spatial profiles distortions.

304 The nonlinear interaction geometry described here is particularly relevant for conversion to the
 305 UV / DUV ranges, where indices of refraction of nonlinear crystals vary rapidly both as a function
 306 of wavelength and angle, yielding large values of walk-off and GVM parameters. Subsequent PFT
 307 compensation might therefore prove useful to efficiently convert broad bandwidth visible pulses
 308 to the UV while conserving a short pulse duration. The peculiar properties of this interaction
 309 geometry call for a reexamination of available nonlinear crystals properties in this wavelength
 310 range, since GVM and walk-off are no longer mechanisms that limit the focusing and/or spectral

311 bandwidth.

312 **Appendix**

313 In this appendix, we provide a detailed spatio-temporal calculation in Fourier space, including
 314 two transverse spatial coordinates and the effects of diffraction and group-velocity dispersion.
 315 We write the complex electric field, $E_\ell(\vec{r}, t)$, using its 4D Fourier transform

$$E_\ell(\vec{r}, t) = \frac{1}{(2\pi)^4} \iiint E_\ell(\vec{k}, \omega) \exp(i(\vec{k} \cdot \vec{r} - \omega t)) d^3k d\omega. \quad (24)$$

316 Within the non-depleted pump approximation, the fundamental field $E_1(\vec{k}, \omega)$, assumed here to
 317 be an ordinary wave, simply obeys the linear propagation equation

$$(-(k_x^2 + k_y^2 + k_z^2) + k_1(\omega)^2)E_1(k_x, k_y, k_z, \omega) = 0, \quad (25)$$

318 where $k_1(\omega) = n_o(\omega)\omega/c$. Within the paraxial wave approximation, we write

$$E_1(k_x, k_y, z, \omega) = A_1(k_x, k_y, z, \omega)e^{ik_1(\omega)z}, \quad (26)$$

319 where $A_1(k_x, k_y, z, \omega)$ is an envelope assumed to vary slowly with respect to z , the propaga-
 320 tion axis. The corresponding expression in Fourier space simply reads $E_1(k_x, k_y, k_z, \omega) =$
 321 $A_1(k_x, k_y, k_z - k_1(\omega), \omega)$, or equivalently $A_1(k_x, k_y, \kappa_z, \omega) = E_1(k_x, k_y, k_1(\omega) + \kappa_z, \omega)$, where
 322 $\kappa_z = k_z - k_1(\omega)$ is small with respect to $k_1(\omega)$. The paraxial wave approximation consists of
 323 keeping terms up to first order in κ_z and up to second order in k_x and k_y . Replacing in Eq. (25)
 324 and neglecting the term in κ_z^2 , we obtain

$$(-k_x^2 - k_y^2 - 2k_1(\omega)\kappa_z)A_1(k_x, k_y, \kappa_z, \omega) = 0, \quad (27)$$

325 or

$$i\kappa_z A_1(k_x, k_y, \kappa_z, \omega) = -i \frac{k_x^2 + k_y^2}{2k_1(\omega)} A_1(k_x, k_y, \kappa_z, \omega). \quad (28)$$

326 Going back to real space for coordinate z , we obtain

$$\frac{\partial A_1}{\partial z} = -i \frac{k_x^2 + k_y^2}{2k_1(\omega)} A_1(k_x, k_y, z, \omega), \quad (29)$$

327 which immediately yields

$$A_1(k_x, k_y, z, \omega) = A_1(k_x, k_y, \omega) \exp\left(-i \frac{k_x^2 + k_y^2}{2k_1(\omega)} z\right). \quad (30)$$

328 We thus recover the well-known expression of the electric field in wavevector space within the
 329 paraxial wave approximation,

$$E_1(k_x, k_y, z, \omega) = E_1(k_x, k_y, \omega) \exp\left(ik_1(\omega)z - i \frac{k_x^2 + k_y^2}{2k_1(\omega)} z\right), \quad (31)$$

330 where the dropped dependence on z in E_1 means that we are considering the field at the entrance
 331 of the crystal, $E_1(k_x, k_y, \omega) = A_1(k_x, k_y, \omega) = E_1(k_x, k_y, 0, \omega)$. Eq. (31) includes the effects
 332 of both diffraction and dispersion and allows to compute the fundamental field $E_1(x, y, z, t)$
 333 through a 3D Fourier transform, so that the second-order polarization $P^{(2)}(x, y, z, t)$ can be
 334 readily calculated, as well as its counterpart in Fourier space.

335 Let us now turn to the propagation of the second harmonic. Assuming that the crystal axis lies
 336 in the xz plane, the propagation equation now reads

$$(-(k_x^2 + k_y^2 + k_z^2) + k_2(k_x, \omega)^2)E_2(k_x, k_y, k_z, \omega) = -\frac{\omega^2}{\epsilon_0 c^2} P^{(2)}(k_x, k_y, k_z, \omega), \quad (32)$$

337 where we have included the second-order polarization as a known source term. Note that, due
 338 to the crystal anisotropy, the quantity $k_2(k_x, \omega) = n_e(\theta(k_x), \omega)\omega/c$ depends on the transverse
 339 component k_x . Indeed, within the paraxial wave approximation we can write $\theta = \theta_0 - k_x/k_2(\omega)$,
 340 where θ_0 is the angle between the z axis and the optical axis and $k_2(\omega) = n_e(\theta_0, \omega)\omega/c$. The
 341 first-order derivative of the wavevector with respect to k_x reads

$$\frac{\partial k_2}{\partial k_x} = \frac{\omega}{c} \frac{\partial n_e(\theta)}{\partial \theta} \frac{\partial \theta}{\partial k_x} = \tan \rho, \quad (33)$$

342 where we have used the well-known relation verified by the tangent of the walk-off angle, ρ ,

$$\tan \rho = -\frac{1}{n_e(\theta)} \frac{dn_e(\theta)}{d\theta} = n_e(\theta)^2 \left(\frac{1}{n_e^2} - \frac{1}{n_o^2} \right) \sin 2\theta. \quad (34)$$

343 Proceeding as for the fundamental beam, we consider the envelope $A_2(k_x, k_y, \kappa_z, \omega) =$
 344 $E_2(k_x, k_y, k_2(k_x, \omega) + \kappa_z, \omega)$, so that Eq. (32) becomes

$$-(k_x^2 + k_y^2 + 2k_2(k_x, \omega)\kappa_z)A_2(k_x, k_y, \kappa_z, \omega) = -\frac{\omega^2}{\epsilon_0 c^2} P^{(2)}(k_x, k_y, k_2(k_x, \omega) + \kappa_z, \omega) \quad (35)$$

or

$$\begin{aligned} i\kappa_z A_2(k_x, k_y, \kappa_z, \omega) &= -i \frac{k_x^2 + k_y^2}{2k_2(k_x, \omega)} A_2(k_x, k_y, \kappa_z, \omega) \\ &+ \frac{i\omega^2}{2\epsilon_0 c^2 k_2(k_x, \omega)} P^{(2)}(k_x, k_y, k_2(k_x, \omega) + \kappa_z, \omega). \end{aligned} \quad (36)$$

Going back to real space for the z coordinate, we obtain

$$\begin{aligned} \frac{\partial A_2(k_x, k_y, z, \omega)}{\partial z} &= -i \frac{k_x^2 + k_y^2}{2k_2(k_x, \omega)} A_2(k_x, k_y, z, \omega) \\ &+ \frac{i\omega^2}{2\epsilon_0 c^2 k_2(k_x, \omega)} P^{(2)}(k_x, k_y, z, \omega) e^{-ik_2(k_x, \omega)z}. \end{aligned} \quad (37)$$

The resolution of this first-order differential equation is straightforward and yields the SHG envelope

$$\begin{aligned} A_2(k_x, k_y, z, \omega) &= \frac{i\omega^2}{2\epsilon_0 c^2 k_2(k_x, \omega)} \exp\left(-i \frac{k_x^2 + k_y^2}{2k_2(k_x, \omega)} z\right) \\ &\int_0^z P^{(2)}(k_x, k_y, z', \omega) \exp\left(-ik_2(k_x, \omega)z' + i \frac{k_x^2 + k_y^2}{2k_2(k_x, \omega)} z'\right) dz'. \end{aligned} \quad (38)$$

In order to calculate the integral along the z axis, we write the explicit expression of the second-order polarization by Fourier transforming the real-space expression $P^{(2)}(x, y, z, t) = \frac{1}{2}\epsilon_0 \chi^{(2)} E_1(x, y, z, t)^2$, which yields the convolution product

$$\begin{aligned} P^{(2)}(k_x, k_y, z, \omega) &= \frac{\epsilon_0 \chi^{(2)}}{2} \iiint E_1(k_{x1}, k_{y1}, z, \omega_1) \\ &E_1(k_x - k_{x1}, k_y - k_{y1}, z, \omega - \omega_1) \frac{dk_{x1}}{2\pi} \frac{dk_{y1}}{2\pi} \frac{d\omega_1}{2\pi}. \end{aligned} \quad (39)$$

Let us introduce the multidimensional wavevector mismatch function, defined as

$$\Delta k(k_x, k_{x1}, k_y, k_{y1}, \omega, \omega_1) = k_1(\omega_1) + k_1(\omega - \omega_1) - k_2(k_x, \omega) - \frac{k_{x1}^2 + k_{y1}^2}{2k_1(\omega_1)} - \frac{(k_x - k_{x1})^2 + (k_y - k_{y1})^2}{2k_1(\omega_1)} + \frac{k_x^2 + k_y^2}{2k_2(k_x, \omega)}. \quad (40)$$

At center frequency and with wavevectors aligned along the z axis, we have $\Delta k(0, 0, 0, 0, 2\omega_0, \omega_0) = 2k_1(\omega_0) - k_2(2\omega_0) = 0$, since we assume that phase matching is fulfilled. However, the mismatch function Δk will depart from zero for other frequency or wavevector values due to the finite spectral and angular acceptance of the phase-matching condition. Eq. (38) now becomes

$$A_2(k_x, k_y, z, \omega) = \frac{i\omega^2 \chi^{(2)}}{4c^2 k_2(k_x, \omega)} \exp\left(-i \frac{k_x^2 + k_y^2}{2k_2(k_x, \omega)} z\right) \iiint E_1(k_{x1}, k_{y1}, \omega_1) E_1(k_x - k_{x1}, k_y - k_{y1}, \omega - \omega_1) \left(\int_0^z e^{i\Delta k(k_x, k_{x1}, k_y, k_{y1}, \omega, \omega_1)z'} dz'\right) \frac{dk_{x1}}{2\pi} \frac{dk_{y1}}{2\pi} \frac{d\omega_1}{2\pi}. \quad (41)$$

The integration over z is straightforward and leads to the introduction of the multidimensional spatio-temporal global response function

$$\Xi(k_x, k_{x1}, k_y, k_{y1}, \omega, \omega_1) = \frac{i\omega^2 \chi^{(2)}}{4c^2 k_2(k_x, \omega)} \exp\left(-i \frac{k_x^2 + k_y^2}{2k_2(k_x, \omega)} z\right) \frac{\exp(i\Delta k(k_x, k_{x1}, k_y, k_{y1}, \omega, \omega_1)z) - 1}{i\Delta k(k_x, k_{x1}, k_y, k_{y1}, \omega, \omega_1)}, \quad (42)$$

which is the spatio-temporal generalization of the global response function, previously introduced in frequency domain only. The second-harmonic field envelope now simply reads

$$A_2(k_x, k_y, z, \omega) = \iiint \Xi(k_x, k_{x1}, k_y, k_{y1}, \omega, \omega_1) E_1(k_{x1}, k_{y1}, \omega_1) E_1(k_x - k_{x1}, k_y - k_{y1}, \omega - \omega_1) \frac{dk_{x1}}{2\pi} \frac{dk_{y1}}{2\pi} \frac{d\omega_1}{2\pi}. \quad (43)$$

345 This expression allows to easily compute the SHG field for any spatio-temporal shape of the
 346 incident field. It can be easily simplified depending on actual experimental conditions. For
 347 example, if we except the case of tightly-focused beams [5] and assume that the crystal thickness
 348 is smaller than the confocal parameter, we can neglect diffraction terms in $k_x^2 + k_y^2$. The mismatch
 349 function then depends only on k_x (at first order), and on the frequency variables, with

$$\Delta k(k_x, \omega, \omega_1) = k_1(\omega_1) + k_1(\omega - \omega_1) - k_2(k_x, \omega). \quad (44)$$

350 This expression can be used to compute SHG taking into account walk-off, group-velocity
 351 mismatch and group-velocity dispersion (GVD). Additionally, neglecting GVD, we can use a
 352 first-order expansion of the wavevectors (Eq. (11) and (12)) and retrieve Eq. (13). Also, note
 353 that Eq. (42) can be simplified by neglecting the slow variation of $k_2(k_x, \omega)$ with respect to k_x
 354 and ω in the prefactor (but of course not in the phase term in Δk where the consequences of this
 355 variation are more dramatic). By setting $k_2 = n_2\omega/c$ in this prefactor, and neglecting diffraction,
 356 we thus easily recover Eq. (8) from Eq. (42).

357 **Funding.** Agence Nationale de la Recherche (ANR-21-CE30-0038-SHOTIME).

358 **Disclosures.** The authors declare no conflicts of interest.

359 **Data Availability Statement.** Data underlying the results presented in this article are not publicly available
 360 at this time but may be obtained from the authors upon reasonable request.

361 **References**

- 362 1. P. Franken, A. E. Hill, C. e. Peters, and G. Weinreich, "Generation of optical harmonics," *Phys. Rev. Lett.* **7**, 118
363 (1961).
- 364 2. K. Tsubakimoto, H. Yoshida, and N. Miyanaga, "600 w green and 300 w UV light generated from an eight-beam,
365 sub-nanosecond fiber laser system," *Opt. Lett.* **42**, 3255–3258 (2017).
- 366 3. O. Novák, H. Turčičová, M. Smrž, T. Miura, A. Endo, and T. Mocek, "Picosecond green and deep ultraviolet pulses
367 generated by a high-power 100 khz thin-disk laser," *Opt. Lett.* **41**, 5210–5213 (2016).
- 368 4. J. Rothhardt, C. Rothhardt, M. Müller, A. Klenke, M. Kienel, S. Demmler, T. Elsmann, M. Rothhardt, J. Limpert, and
369 A. Tünnermann, "100 w average power femtosecond laser at 343 nm," *Opt. Lett.* **41**, 1885–1888 (2016).
- 370 5. D. A. Kleinman, A. Ashkin, and G. Boyd, "Second-harmonic generation of light by focused laser beams," *Phys. Rev.*
371 **145**, 338 (1966).
- 372 6. A. Smith, D. Armstrong, and W. Alford, "Increased acceptance bandwidths in optical frequency conversion by use of
373 multiple walk-off-compensating nonlinear crystals," *JOSA B* **15**, 122–141 (1998).
- 374 7. A. Weiner, A. Kan'an, and D. Leaird, "High-efficiency blue generation by frequency doubling of femtosecond pulses
375 in a thick nonlinear crystal," *Opt. Lett.* **23**, 1441–1443 (1998).
- 376 8. S. M. Saitiel, K. Koynov, B. Agate, and W. Sibbett, "Second-harmonic generation with focused beams under
377 conditions of large group-velocity mismatch," *JOSA B* **21**, 591–598 (2004).
- 378 9. H. Wang and A. M. Weiner, "Efficiency of short-pulse type-i second-harmonic generation with simultaneous spatial
379 walk-off, temporal walk-off, and pump depletion," *IEEE Journ. Quant. Elec.* **39**, 1600–1618 (2003).
- 380 10. Y. Takagi, Y. Yamada, K. Ishikawa, S. Shimizu, and S. Sakabe, "Ultrafast single-shot optical oscilloscope based on
381 time-to-space conversion due to temporal and spatial walk-off effects in nonlinear mixing crystal," *Jap. Journ. Appl.*
382 *Phys.* **44**, 6546 (2005).
- 383 11. N. A. Chaitanya, A. Aadhi, R. P. Singh, and G. K. Samanta, "Type-i frequency-doubling characteristics of high-power,
384 ultrafast fiber laser in thick bibo crystal," *Opt. Lett.* **39**, 5419–5422 (2014).
- 385 12. N. A. Chaitanya, A. Aadhi, S. C. Kumar, M. Jabir, G. Samanta, and M. Ebrahim-Zadeh, "Frequency-doubling of
386 femtosecond pulses in "thick" nonlinear crystals with different temporal and spatial walk-off parameters," *IEEE Phot.*
387 *Journ.* **8**, 1–13 (2016).
- 388 13. J. Hebling, "Derivation of the pulse front tilt caused by angular dispersion," *Opt. Quant. Elec.* **28**, 1759–1763 (1996).
- 389 14. S. Akturk, X. Gu, P. Gabolde, and R. Trebino, "The general theory of first-order spatio-temporal distortions of
390 gaussian pulses and beams," *Opt. Exp.* **13**, 8642–8661 (2005).
- 391 15. R. Danielius, A. Piskarskas, P. Di Trapani, A. Andreoni, C. Solcia, and P. Foggi, "Matching of group velocities by
392 spatial walk-off in collinear three-wave interaction with tilted pulses," *Opt. Lett.* **21**, 973–975 (1996).
- 393 16. A. M. Schober, M. Charbonneau-Lefort, and M. M. Fejer, "Broadband quasi-phase-matched second-harmonic
394 generation of ultrashort optical pulses with spectral angular dispersion," *JOSA B* **22**, 1699–1713 (2005).
- 395 17. J. J. Huang, L. Y. Zhang, W. C. Zhang, S. R. Yan, S. Z. Pu, and W. X. Ren, "Theory of second harmonic generation
396 of ultrashort pulses for collinear achromatic phase matching," *JOSA B* **30**, 431–438 (2013).
- 397 18. B. Willenberg, F. Brunner, C. R. Phillips, and U. Keller, "High-power picosecond deep-uv source via group velocity
398 matched frequency conversion," *Optica* **7**, 485–491 (2020).
- 399 19. J. P. Torres, M. Hendrych, and A. Valencia, "Angular dispersion: an enabling tool in nonlinear and quantum optics,"
400 *Adv. Opt. Photon.* **2**, 319–369 (2010).
- 401 20. P. Nuernberger, K. F. Lee, and M. Joffre, "Femtosecond spectroscopy from the perspective of a global multidimensional
402 response function," *Acc. Chem. Res.* **42**, 1433–1441 (2009).
- 403 21. M. Joffre, J. O. White, D. Hulin, A. Migus, E. Toussaere, R. Hierle, S. Gauvin, and J. Zyss, "Femtosecond
404 ultrabroad-band frequency mixing in mna and kdp thin crystals," *Nonlinear Opt.* **11**, 5–12 (1995).
- 405 22. L. Lepetit and M. Joffre, "Two-dimensional nonlinear optics using fourier-transform spectral interferometry," *Opt.*
406 *Lett.* **21**, 564–566 (1996).
- 407 23. N. Belabas and M. Joffre, "Visible-infrared two-dimensional fourier-transform spectroscopy," *Opt. Lett.* **27**, 2043–2045
408 (2002).
- 409 24. T. Brabec and F. Krausz, "Nonlinear optical pulse propagation in the single-cycle regime," *Phys. Rev. Lett.* **78**, 3282
410 (1997).
- 411 25. M. Hanna, X. Délen, L. Lavenu, F. Guichard, Y. Zaouter, F. Druon, and P. Georges, "Nonlinear temporal compression
412 in multipass cells: theory," *J. Opt. Soc. Am. B* **34**, 1340–1347 (2017).
- 413 26. T. Lang, A. Harth, J. Matyschok, T. Binhammer, M. Schultze, and U. Morgner, "Impact of temporal, spatial and
414 cascaded effects on the pulse formation in ultra-broadband parametric amplifiers," *Opt. Exp.* **21**, 949–959 (2013).